PERGAMON

International Journal of Multiphase Flow 26 (2000) 1419–1438

International Journal of Multiphase Flow

www.elsevier.com/locate/ijmulflow

Motions of dispersed beads obtained by particle tracking velocimetry measurements Part II

S.J. Haam [1], R.S. Brodkey*

Department of Chemical Engineering, The Ohio State University, 140 West 19th Avenue, Columbus, OH 43210-1180, USA

Received 9 February 1997; received in revised form 23 December 1997

Abstract

Particle tracking velocimetry was successfully used to study the three-dimensional solids movement of large dispersed beads in a vertical column. For the large beads, overlap was a major limitation, especially at high bead concentrations. Thus, an additional image enhancement algorithm for particle decomposition was developed as a preprocessor. The beads experienced high axial and radial fluctuation values; but, these increases were less than for the fluid phase itself. This is, no doubt, a result of the higher inertia of the beads relative to the fluid. The bead fluctuations are less for the radial component than for the axial component, which is similar to that for the fluid phase. From the results of the histogram analysis, the higher bead concentrations period provided broader and more scattered distributions except for the initial transport period. Finally, comparisons were possible with the data obtained and predictions from a variety of theoretical approaches.

Keywords: Dispersion; Solid–liquid flow; Multiphase flow; IR matching; LDA; PTV

1. Introduction

In part I, the level of turbulence in the fluid phase in the presence of beads was investigated.

* Corresponding author. Tel.: +1-614-292-2609; fax: +1-614-292-3769.
E-mail address: brodkey.1@osu.edu (R.S. Brodkey)
[1] Present address: Department of Chemical Engineering, Yonsei University, Seoul, South Korea.

0301-9322/00/$ - see front matter
PII: S0301-9322(99)00095-6

The turbulence in the fluid was found to be higher with beads present than for the fluid alone. In this second part, it is important to establish the turbulence associated with the bead motions. Models are needed to describe the interactive motions of both phases and their characteristics. The data on bead motions were obtained using particle tracking velocimetry (PTV). The same large spherical molded polymethyl methacrylate (PMMA) beads ($d_p = 4.765$ mm) were used in the index of refraction matching fluid, *p*-cymene. The index of refraction match was excellent between the fluid and the dispersed solid, thus, to use the PTV technique, some of the beads were marked with dye. Again, to avoid a solids circulation system, the experiments were obtained under transient flow conditions. The concentration of beads present as a function of time was also determined from the PTV experiments. Many independent transient runs were made to insure that a statistical significant sample was obtained.

The present paper is also an abbreviated version. A more complete version can be found at the URL, given in the reference list as Haam and Brodkey (1998). The full details for the study can be found in dissertation by Haam (1996).

2. Literature review

Govan et al. (1989) studied particle motions in a solid–air turbulent pipe flow. An axial view was used with high-speed cinema (400 frames/s) and three different sizes of glass particles ($d_p = 110$, 250 and 550 μm). The radial trajectories of particles were measured, but the number was small. Mondy et al. (1986) used a high-speed video system with X-rays for observing particle dynamics of free falling particles in concentrated suspensions. However, these measurements were limited to creeping flow and the local fluctuations of particles were not determined. Nouri and Whitelaw (1992) measured the mean and rms velocities of particles by using laser Doppler anemometry (LDA) in solid–liquid turbulent flow in a fully baffled stirred mixing vessel. They matched the index of refraction between fluid phase and dispersed particle phase and were capable of observing concentrations upto 2.5%. The range of the particle sizes that they used was from 232 to 725 μm. They measured the axial and radial mean and rms velocities of the particle phase at different locations in the vessel. They found that the particle fluctuating velocities of the heavier particles were lower than those of lighter particles and that the axial and radial mean velocities decreased with increasing particle concentration. The concentration effect did not influenced the particle turbulence. Koh et al. (1994) performed a some what similar IR match experiment to measure the particle velocities in a concentrated suspension. They used LDA (as used in part I of this study to measure the fluid velocity) to measure small (30–89 μm) polystyrene particles that were both density and IR matched. Small imperfections in the particles were used as the source of the LDA signals. They did not measure the fluid velocity. However, since the particles were neutrally buoyant, the fluid velocity should have been very nearly the same as the particles. Unlike our particles, their's would be considered small and should dampen the turbulence fluctuations; however, this could not be ascertained as their study was restricted to laminar flow. The value of this study for the present work is the care and full considerations made of the problem of IR matching.

The available theoretical approaches for the interaction of large particles and fluid have not been completely tested with experimental data due to the experimental difficulties of measuring turbulent intensities of the two phases, simultaneously. Most of the approaches for turbulent flows, laden with large particles, are numerical studies using the k–ε turbulence model for the continuous phase to calculate particles–turbulence interaction (Shuen et al., 1985; Shriber et al., 1990) or the turbulent kinetic energy balance (Parthasarathy and Faeth, 1990; Yuan and Michaelides, 1992). Parthasarathy and Faeth (1990) studied the turbulent dispersion of particles in a homogeneous turbulent field both experimentally and theoretically. They calculated the turbulent velocities for particles and liquid based on a random-walk computation with a turbulent kinetic energy balance. Yuan and Michaelides (1992) proposed a theory to consider the mechanisms contributing turbulence in dispersed two-phase flow as: (1) dissipation of turbulent kinetic energy and (2) vortex shedding due to wakes behind particles. Yarin and Hestroni (1994) have used the modified turbulent mixing length and turbulent kinetic energy approach to predict the turbulent intensity level of the carrier fluid and the particles with particle size. The results of this proposed theory were in fairly good agreement with the experimental data (Tsuji et al., 1984).

3. Experimental

3.1. Stereo-visualization system for dispersion column study

The basic flow system is the same as that described in part I. More details on the flow facility can be found in Haam and Brodkey (1998) and Haam (1996). Only the briefest of information about the stereoscopic imaging system used in this study will be given here.

3.1.1. Dyeing of beads

About 15% of the spherical molded polymethyl methacrylate (PMMA) beads used as the solid phase were dyed for tracking. The percentage level was selected to provide the maximum number of visual beads and still minimize the complexity of overlapping bead images. A commercial dye for cloth (Rhoda-calcomine B) was used to dye the beads dark red. The illuminating method required that the beads absorbed the light and appear as dark areas on a light background. A CCD camera with a SVHS, VCR recorder were used to record the image pairs. For three-dimensional flow visualization, a single camera with a mirror arrangement was used to obtain the two simultaneous stereo views rather than using two synchronized cameras. The density of PMMA is 1190 (kg/cm^3), which is heavier than the working fluid (*p*-cymene).

3.1.2. Lighting system

The lighting had to be optimized for the system by considering bead size, bead type, system size, flow condition and so forth. Commercial blue fluorescent light sources and blue semi-transparent plastic sheets resulted in successful images by limiting the light frequency range. In addition, a semi-opaque filter paper was used to smooth out light intensity variation and produce a uniform illumination throughout the flow field. Four fluorescent lights were used. The set-up is shown in Fig. 1.

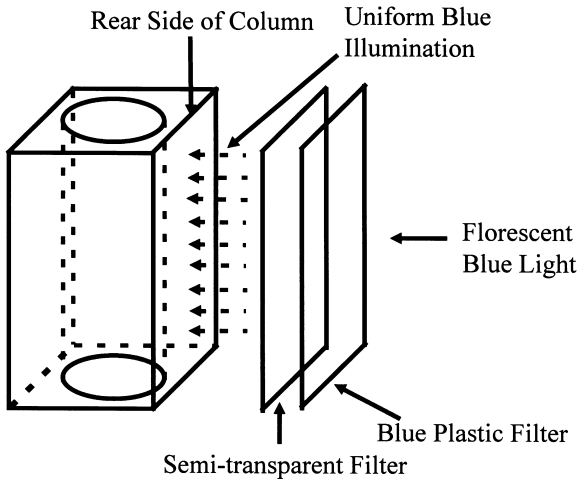

Fig. 1. Schematic of lighting system.

3.1.3. Mirror alignment for stereoscopic images

As shown in Fig. 2, a mirror arrangement was located in front of the camera lens. Guezennec et al. (1994) tested the PTV system using synthetic images and varied the stereo angle. They found that an angle of 90° produced the lowest errors from the stereo matching step. Although the mirror alignment system has a drawback of reducing the horizontal resolution of the images by 50% when compared to a two camera system, it does provide exact synchronization and needs only a single image acquisition board. In our case, since half vertical resolution was used so we could obtain 60 Hz time resolution with a standard CCD

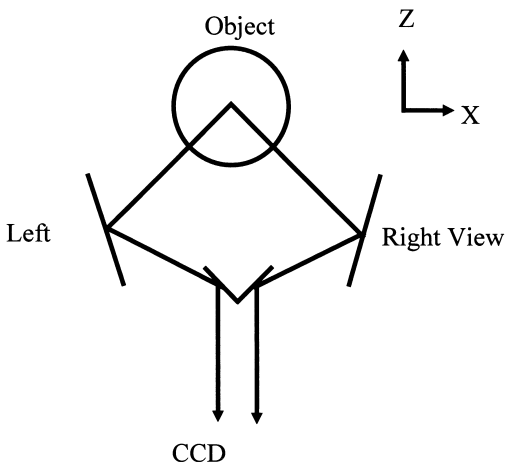

Fig. 2. Mirror alignment for stereo visualization.

camera, the net result was that individual pictures were about square as was the area being viewed.

3.1.4. Lens and recording system

A single Pulnix CCD video camera was used with a Cannon TV-zoom lens (17–102 mm). The resolution of the CCD camera is nominally 512^2 pixel array running in an interlaced mode at a full frame rate of 30 Hz. By using the interlaced mode, the CCD camera records even and odd images at a frame rate of 60 Hz and stores the image data as an interlace image at a frame rate of 30 Hz. To increase the frame rate from 30 to 60 Hz to prevent streaks and provide better time resolution, these interlaced even and odd images were separated by the imaging board and each saved as an individual image with a time interval of 1/60 s. Even though the separation of interlaced image reduces the vertical resolution by half, it has the advantage of providing double the camera speed. Since one half horizontal resolution was used with the mirror system, the net result was individual images of about 256^2 size. This final resolution used was more than adequate because the beads were large. The time sequential data were stored on VCR tape using a Panasonic Hi-Fi SVHS-AG7355 video recorder. This video-recording device provides RS-232C interface mode (Model No. AG-IA232TC) between the VCR and the computer, so that the data acquisition and VCR operation are fully automated by software written in C.

3.2. 3D PTV system

The goal of the 3D-PTV system is to extract the full three-dimensional velocity field from time sequences of single exposed stereo images. The technique developed by Guezennec et al. (1994) is the methodology used in this study. The steps taken will be described here in their briefest outline form and will emphasize only the deviations from the norm. The readers should consult Haam and Brodkey (1998), Haam (1996) and Guezennec et al. (1994) for more details on the normal steps in the technique.

The system requires a careful calibration step because such experiments usually have multiple media with significant index of refraction mismatches, which can cause serious optical aberrations. Included are possible camera misalignments, lens distortions, etc. The calibration procedure normally uses an in-situ calibration method developed by Choi et al. (1992). However, in the dispersion column a target could not be used; thus, the calibration data were acquired using a ray tracing method and the calibration algorithm was subsequently used to obtain the least square fit transformation function. For accurate ray tracing, scales for calibration were attached on the front and rear sides of both stereo views in both the vertical and horizontal directions.

The actual visualization step involves data acquisition by using the CCD camera and recorder. After image acquisition on video tape, the images were digitized. An image board was used to convert the physical images from the VCR with a fully automated operation. The software was capable of pinpointing the frame number and activating the image grabber to digitize and save up to 16 time sequential images automatically. A Super VGA graphic card was used for video display. The image grabbing rate is 30 Hz in an interlaced mode composed

of a combination of even and odd lines. These even and odd fields were separated and stored providing a time sequence at 60 images/s.

Image pre-processing was performed to standardize the images and facilitate the task of locating beads. Image pre-processing is the image enhancement steps used to improve the digitized images prior to the bead identification and tracking process. The specific image preprocessing steps were image splitting and doubling, histogramming (to separate the particles from the background), stretching (to use the maximum light level range), subtraction (to remove noise and constant background information), filtering (to assure the image is sharp) and binary digitization (to obtain the final black and white image). A single image contained both stereo images (left and right) since a single camera with a mirror was used. Since the PTV algorithm finds the particle locations and tracks of both stereo images, the stereo images had to be split. Also, a single image contained both even and odd fields with a time interval of 1/60 s, so that the images, in addition, had to be separated into even and odd fields. Since the picture resolutions of the separated even and odd images was decreased by 50% vertically, for convenience, these images were doubled to maintain the same aspect ratio by simply repeating each line. Fig. 3(a) shows an example of the raw image containing both stereo views. The even field split images are shown in Fig. 3(b) for the doubled stereo image. The gray level of the final images had to be inverted since the PTV algorithm requires the image contain a dark background with bright particles (as shown in Fig. 4).

Fig. 4 is used to show the additional steps involved in the preprocessing. For best result in the subtraction process, it is important that the background image and image with particles are recorded under identical experimental conditions. In Fig. 4(a), the background noise of the median filtered image was removed by using subtraction. For a high concentration of large beads, bead overlapping each view contributes the major error in identification of bead location. The decomposition step decomposed approximately 90% of the total overlapped beads. This step provided a more suitable image for the subsequent decomposition algorithm in the PTV code. The decomposition step increases the number of tracks and reduces the error in locations by eliminating complex multibead overlapped images. The basic concept of the additional pre-decomposition process involves image correlation with a particle template, which is similar to that in the PTV algorithm. However, it uses a different correlation coefficient. Fig. 4(b) shows the result of this procedure where Fig. 4(a) is the starting image. In Fig. 4(b), the centroids of the overlapped particles appear as bright dots and the surrounding overlapped area as the darker region.

The stretching processes commonly used where the distribution of the gray level in the image does not cover the full brightness range and produces poor contrast between the particles and the background. This process was done after the pre-particle decomposition step shown in Fig. 4(b). Fig. 4(c) shows the quality of the enhanced image using the stretching process. The stretching resulted in more distinct peaks between the particles and background. Thresholding sorts the image into background and particle pixels by use of the histogram of gray levels. An example of the binary digitization process is shown in Fig. 4(d). After the thresholding process, the two stereo images were scanned line by line and from top left to bottom right. During this process, the second particle decomposition step is performed. The 2D particle locations are shown in Fig. 4(e) for the marked area in Fig. 4(a). The particle tracking process is the heart of the PTV approach and is designed to obtain the path and the velocity vectors of the beads.

The optimum number of particles to betracked is important for accuracy. Based on the study by Guezennec et al. (1994), the optimal particle seeding density is a compromise between the accuracy of the data and the time to process an image. For our large beads, the algorithm was capable of tracking up to 200 beads as a maximum. If the number of beads was much larger than this, the particle decomposition processes became excessive. The particle tracking step uses a sequence of frames to establish the most probable particle path (position versus time) for each particle. This is done independently for the left and the right stereo views. No prior knowledge of the flow is required, except for an upper bound estimate on the maximum distance traveled by a particle between two successive frames. Stereo matching is used to reconstruct the 3D coordinates from the 2D projections of the stereo views (left and right). The

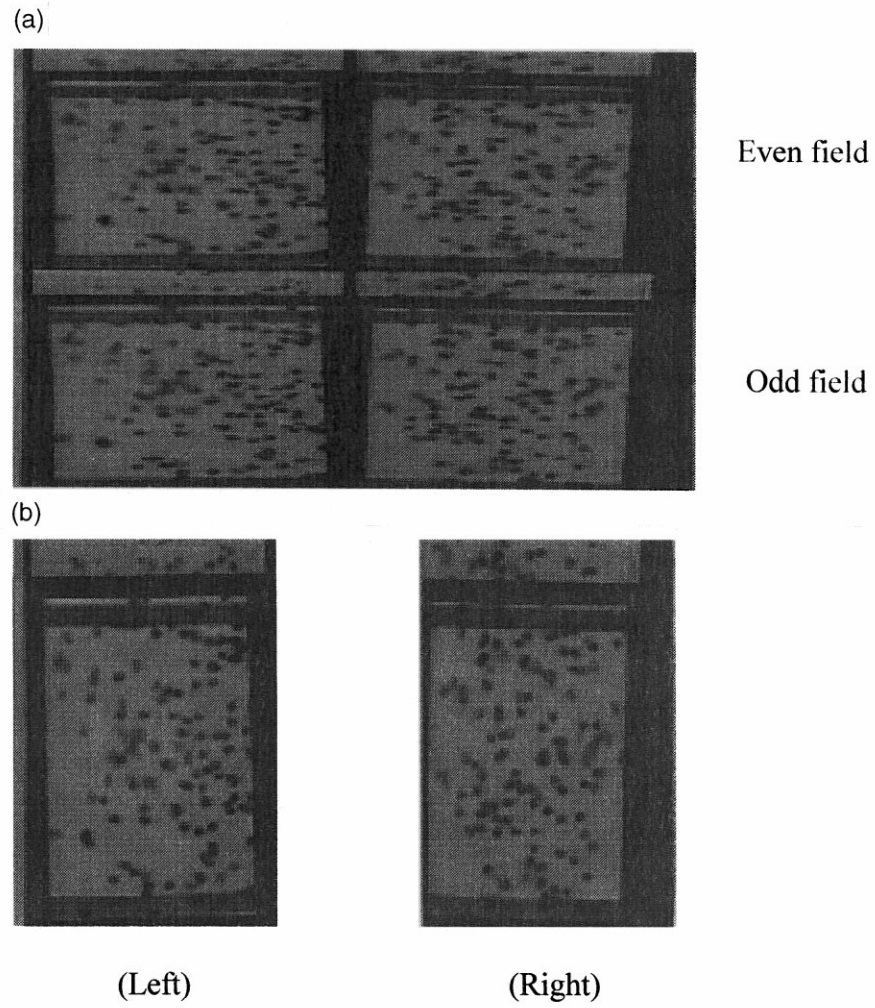

Fig. 3. (a) Raw image containing stereo views. (b) Image doubling.

stereo matching algorithm uses the particle tracks as obtained from the five frames in each stereo view instead of using individual particle locations. After the stereo matching algorithm reconstructs the best 3D tracks from the 2D tracks, a final validation is performed using an adaptive Gaussian window (AGW) filtering. Neighboring velocity vectors computed from each particle track are compared to a smooth local 3D interpolated value, with a 3D Gaussian filter. If one velocity vector is too different from its neighborhood average, it is rejected as being possibly erroneous since neighboring velocity vectors must be relatively similar with respect to the scale of the flow. The width of the 3D Gaussian filter is automatically adjusted as a function of the data density. The entire process is then repeated by advancing the frame count by one.

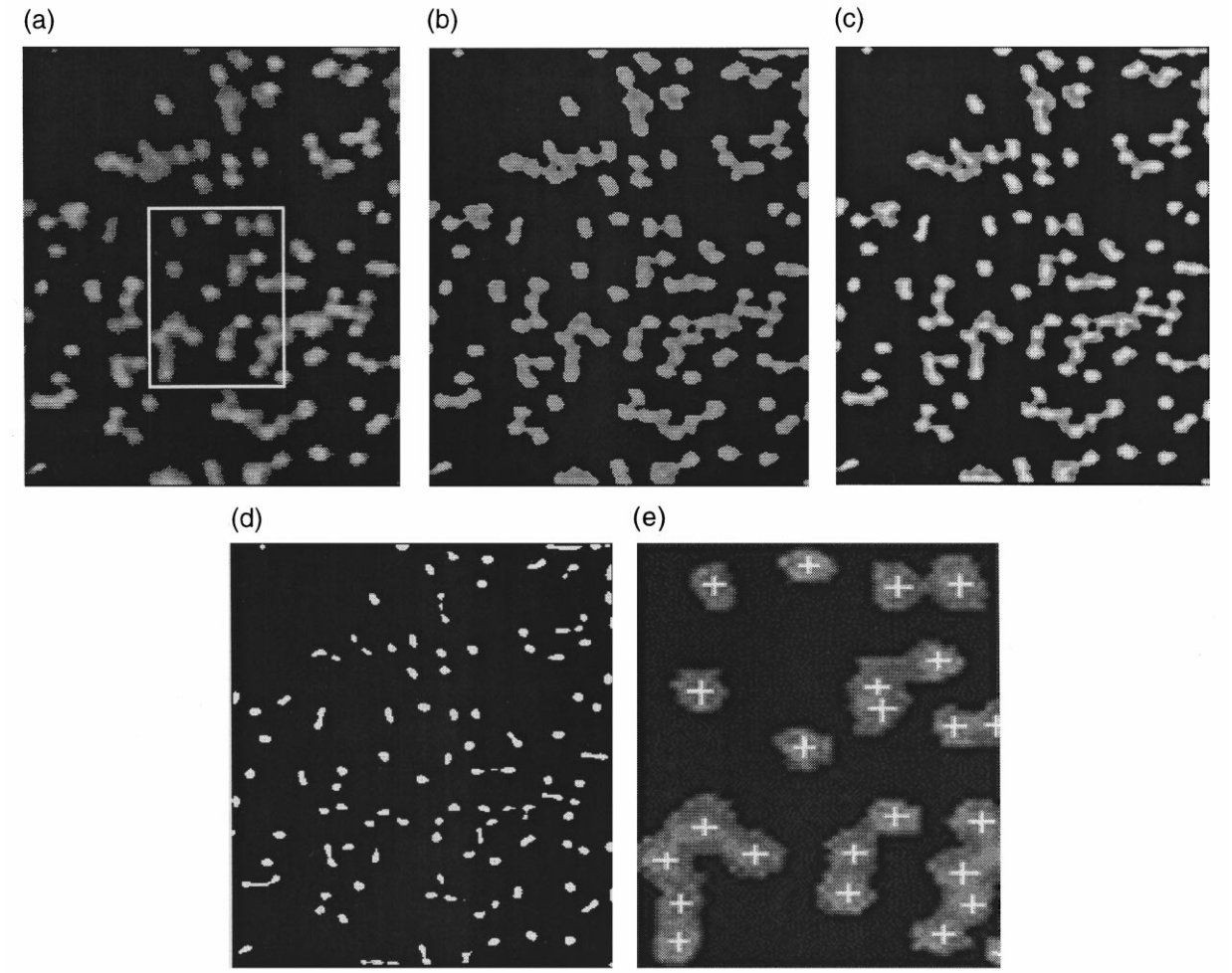

Fig. 4. (a) Subtracted image. (b) Decomposition of overlapping particles using pre-particle decomposition. (c) Stretched gray level image. (d) Binary digitized image. (e) Results of 2D particle location.

4. Data, theory and discussion

4.1. PTV velocity of solid phase during dispersion

4.1.1. Ensemble averaged mean and rms velocities

Based on the ensemble averaged concentration–time profile (Fig. 2, part I), the time periods corresponding to the concentrations were defined (see part I for the definitions). For each individual concentration–time profile (nearly 70 runs), the image data were analyzed for these same time periods. For each, the velocity vectors and corresponding positions were obtained using the PTV algorithm. Finally, the ensemble averaged 3D mean and rms velocities were computed. In part I, the LDA measurement were at a single point along the center-line of the column. The PTV measurements, in contrast, are over a volume that includes the LDA point at the center. In this volume of the flow, the mean was relatively flat as indicated in part I.

The data from the PTV algorithm were transformed from Cartesian coordinates (native to the PTV system) to the cylindrical coordinates (r, θ and z) of the column. The mean and rms velocities of large beads and of the fluid (from part I) are presented in Table 1 based on the corresponding time periods. As was done in part I, the time subdivisions used by Haam (1996) were combined into one division for clarity of presentation in this paper. Although the LDA data were obtained for both the large and small particles as reported in part I, the PTV data were only obtained for the large beads. In Table 1, for the large beads, the axial mean velocities of the beads are about one-quarter to one-half of the liquid phase in each corresponding concentration period. Recall that these beads are heavier than the surrounding fluid. In the initial transporting period (I), the mean velocity of the beads are the highest, which supports the idea that the beads were accelerated by the upward flow before they were fully dispersed. After the beads were dispersed (periods II and III), the mean velocities of the beads were similar. For the radial mean velocities of the beads were very closed to zero due to the symmetrical.

For the solids, the axial rms values of the initial period (I) was usually lower than those of the fully dispersed periods (II and III), but the radial rms values were slightly higher. These results can be explained by the visual observations of the motions of the beads in each time period. The axial fluctuations of the beads in the initial period should be lower since at the

Table 1
Overall comprarisons of mean, rms, skewness and flatness for fluid and solid phases

Unit (cm/s)	Fluid phase				Solid phase (beads)					
	Axial		Radial		Axial				Radial	
	Mean	rms	Mean	rms	Mean	rms	Skewness	Flat	Mean	rms
Period I	20.75	8.75	1.53	4.50	11.76	5.16	−1.05	3.74	0.12	4.01
Period II	25.22	7.94	0.98	3.26	7.98	5.86	−0.55	2.84	−0.02	3.62
Period III	28.43	4.41	0.81	2.84	7.46	4.87	−0.39	2.70	0.17	3.32
Period IV	28.38	3.29	0.74	3.05	–	–	–	–	–	–

initial high-concentration, slug flow conditions did not allow the beads to be fully dispersed. However, after the beads were dispersed, the axial rms values should be higher since the gravitational force on the beads was effective along the axial direction. Recall, that the initial condition in the radial direction was different. Initially, the beads were spread in the radial direction. Thus, the radial rms values could be higher in the initial periods. For periods II and III, the higher concentration provided the higher axial rms values of the beads but the differences were relatively less than that for the fluid phase. Similar results were found for the radial fluctuations, but the concentration effect on the bead fluctuation was less for the radial component than for the axial component. From the results, it is concluded that the large, heavy beads take turbulent energy from the mean flow of the fluid and transfer it to the fluid phase. The mechanism is believed to be a result of the bead wake effect, however, the beads themselves are relatively insensitive to added movement because of their inertia and bead–bead interactions.

4.1.2. Histogram analysis

Histograms were used to compare the bead motions within the different concentration periods. For bead velocities, since there were none present during period IV, a different histogram technique (from that used in part I) had to be used. The x-axis of the histogram was taken as

$$X = U_p - (\langle U_{eff} \rangle - \langle U_t \rangle)/s$$

$\langle U_{eff} \rangle$ denotes the average fluid velocity across the column with the beads present. The values of $\langle U_{eff} \rangle$ were calculated from the concentration data of each time period and the ensemble average of U in period IV, when the beads were not present. It is, in effect, a volume averaged velocity between the beads. The term, s is the standard deviation and U_t is the terminal velocity of the bead calculated from the Richardson and Zaki equation. The y-axis was often normalized on the maximum value of and thus would be unity.

4.1.1.1. Axial velocities of the beads. Fig. 5 shows the number histogram for the axial velocities for all time-periods. The skewness and flatness of the corresponding histograms were calculated and are shown also in Table 1. The histograms vary mostly in negative tails ($X < 0$). The negative values of the skewness support this observation. For the calculated values of ($\langle U_{eff} \rangle - U_t$), $\langle U_{eff} \rangle$ is based on the assumption of a uniform distribution of the solid phase on the average and U_t is calculated based on a single bead at the fluid condition of $\langle U_{eff} \rangle$. However, in the actual experiments, the instantaneous observation of the dyed beads was that they were not always perfectly distributed in the fluid, and sometimes large clumps of dyed beads existed at a localized radial position. Such clumps of beads would often move as a whole. Since only 15% of the beads were marked and we had no means of observing the unmarked beads, we do not know if these instantaneous local regions of dyed beads was representative of the population as a whole. We do know, however, that the ensemble averaging process would even out the distribution. The wakes (which represent lower velocity regions), would cause beads near the wake to experienced even lower velocities.

The total fluctuation energy [$\sim \sum(U_p - \langle U_p \rangle)^2$], with the ρ and 1/2 factor left out, was used

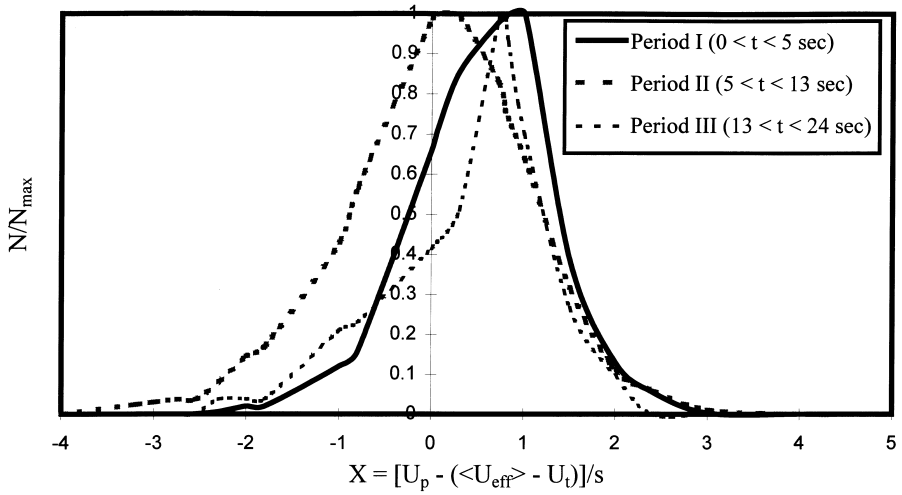

Fig. 5. Comparison of number histograms with beads for all axial particle velocities.

to investigate the differences in the turbulent level of the solid bead phase in the various concentration periods. Here, $\langle U_p \rangle$ denotes the local ensemble averaged mean velocity in the period being considered. The overall rms values and turbulent intensities were previously

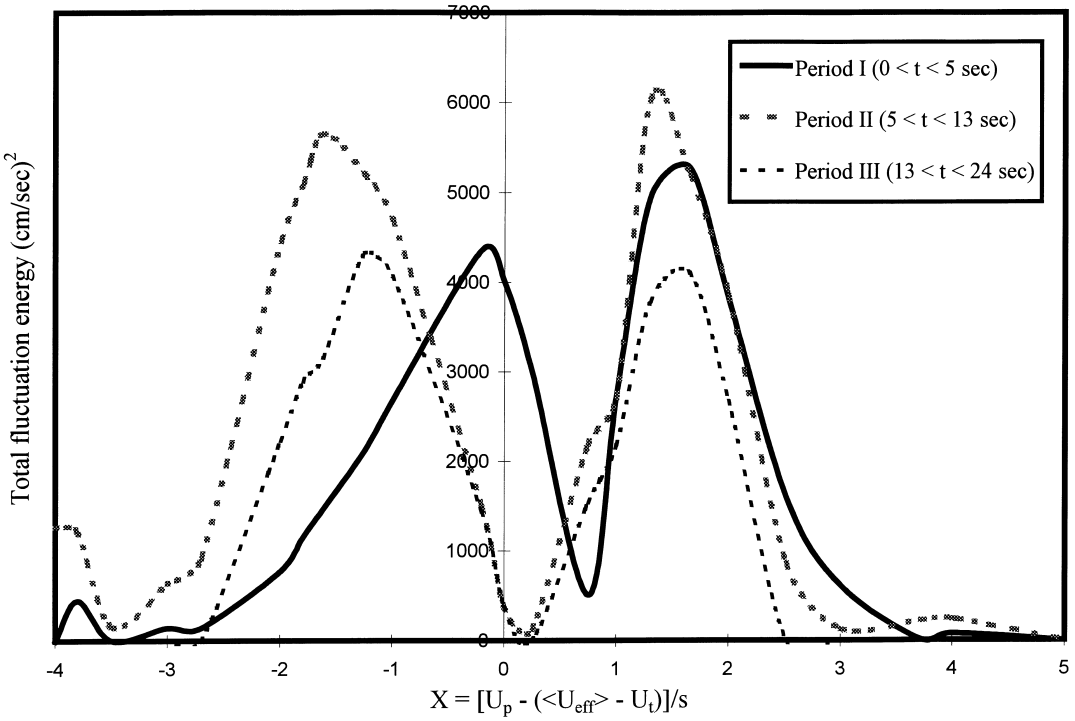

Fig. 6. Comparison of total fluctuation energy histograms with beads for all axial particle velocities.

presented in Table 1. As cited in part I, the same total number of events in the different time periods were required for the total fluctuation energies of various periods to be compared. Period I had the highest number of events due to its being the highest concentration period, so that the total fluctuation energies in other periods were multiplied by the ratio, 'number of events in period I/number of events in periods being considered'. Fig. 6 is the histogram comparisons of the total fluctuation energies on the same number of events basis. Again, for convenience, the y-axis for energy is actually U^2 in units of $(\mathrm{cm/s})^2$. The histograms of total fluctuation energies of the initial periods were first compared. In Fig. 6, the histogram of period I shows the narrowest distribution even though it is at the highest mean velocity. The level of the total fluctuation energy of period I is slightly lower than that of the other periods except for period III which has a very low concentration. For the fully dispersed bead periods (II and III), the total fluctuation energies increased with increase in the bead concentration. In contrast to Fig. 6, Fig. 7 contains the total energy histogram based on the same number (not relative to an average, but the actual velocity squared without the density or the 1/2 factor). The total energy distribution is near Gaussian in shape, but shifted to $X > 0$, and is a relatively narrow distribution for period I (initial slug flow), which also has the highest peak. For period III (low concentration), the distribution of the total energy is narrow since the fluctuation of the beads are not effectively influenced due to the low concentration. For the other time periods, the distributions are broader. The distribution of period I is not as broad as the distribution of period II where the beads were fully dispersed.

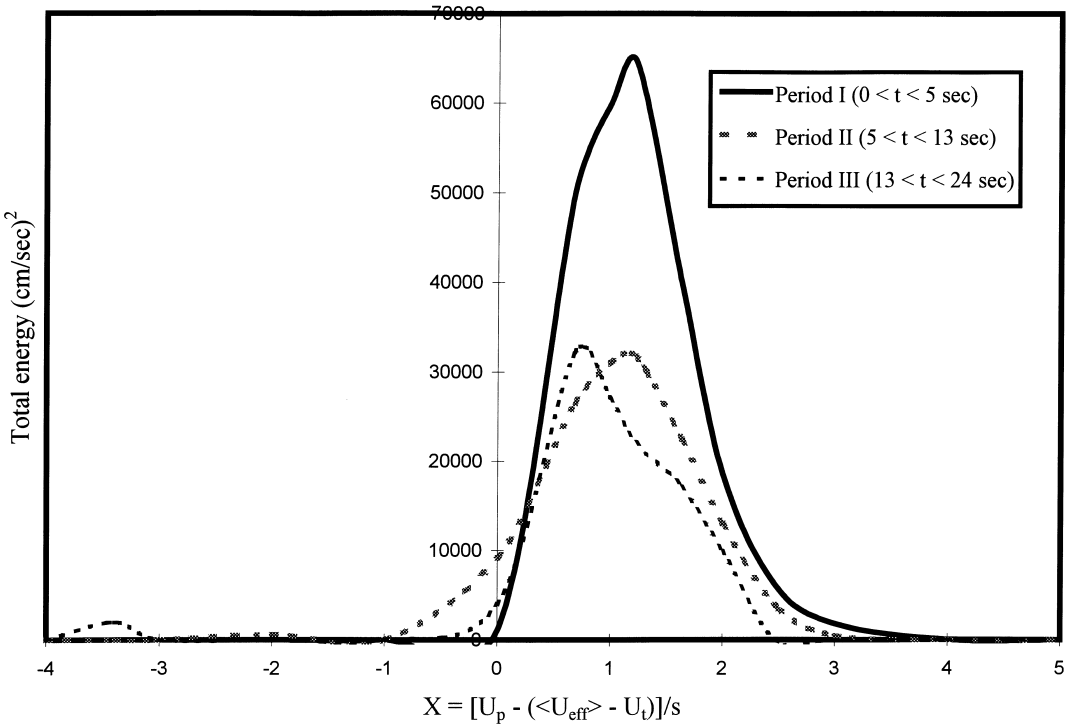

Fig. 7. Comparison of total energy histograms with beads for all axial particle velocities.

4.1.1.2. Radial velocities of the beads. For the radial velocities, the same normalization as for the axial velocities was not used. Instead, $U_p - \langle U_p \rangle$ was used for the x-axis where $\langle U_p \rangle$ is an ensemble average of U_p. As in part I, these figures are not included here (see Haam and Brodkey, 1998 for the figures). For the most part these figures are similar to those for the axial. However, there are some differences; for example, the histograms for the total fluctuation energy are bimodal. Unlike the axial case, the radial histogram for period I is broader than that for the axial case. This means there is a wider range of fluctuations and does not necessarily means higher radial fluctuations. As already noted, the beads were already spread in the radial direction as a results of the experimental design. For period I, the initial transporting period, the overall rms values were higher than the other periods. The reason of the higher rms value for this period was due to its higher amplitude. This can be seen in Table 1 which represents the data of skewness and flatness in the different time periods. The flatness of period II is the highest. Needless to say, the concentration level also provides more active bead interactions and causes higher fluctuation of the beads. The total energy histograms are also symmetrical and the histograms are almost similar as the total fluctuation histograms because the ensemble average of radial U_p is very close to zero.

5. Comparison with theories

For two-phase systems, models are needed to describe the relative local fluctuations of solids and fluid for operations involving surface phenomena. Such models need to be tested with experimentally measured data. The present work provides the only direct measurements of the rms fluctuations of large nonbuoyant solids together with measurements of the rms fluctuations of the fluid in the presence of such solids. The next step is to find any specific theoretical approaches that can describe the dispersion of solid particles in a solid–fluid flow and their relative motion to the flow.

5.1. An integral approach for a vertical system using the law of Richardson and Zaki

The overall approach accounts for the effect of the presence of particles as a two-phase mixture with an effective viscosity. Based on the assumptions of steady state and a dilute system, the relative velocity of the two-phases are

$$U_r = U_f - U_p = U_t(1 - \varepsilon_p) f(\varepsilon_p)$$

where U_f is the velocity of fluid in the area of the beads but not close enough to be affected by the beads, U_p is the velocity of the beads, U_t is terminal velocity of the beads from Richardson and Zaki (R–Z) correlation, ε_p the volume fraction of beads and $f(\varepsilon_p)$ is a function of the effective viscosity given by $\mu_e = \mu_f / f(\varepsilon_p)$.

In all of the theoretical studies, the various authors did not account for turbulence that might result from the boundary layer on the forward part of the beads or enhanced turbulence due to the higher velocity between the beads. In our measurements in part I, which measured all the fluid at the LDA intersection point, higher turbulence that might exist in the fluid due

to the enhanced velocity would have been measured. The resolution would prevent the boundary layer turbulence on the beads from being measured. Note that none of these effects can be separated from the wake effect and all are obtained as a single measurement.

Using the empirical law by R–Z, $f(\varepsilon_p)$ can be expressed as, $f(\varepsilon_p) = (1-\varepsilon_p)^{0.39}$, the relative velocities for different bead concentration periods are calculated and shown in Table 2. In this table, the period subdivisions have been retained to provide the more detailed information on the concentration effect. The particle volume fractions and the relative velocities are given for each period. The velocity of the continuous phase, U_f was not directly measured from the LDA. However, U_f can be considered to bean effective velocity of fluid passing through the bead period such as

$$U_f = U_{sf}\left[\frac{A_f}{A_f - A_p}\right] = \frac{U_{sf}}{1-\varepsilon_p}$$

where U_{sf} is the superficial velocity of the fluid in the column without beads, A_f the cross sectional area of the empty column (without beads) and A_p is the average projected cross sectional area of the beads at the given concentration.

U_f is calculated with U_{sf} from the LDA data and U_p from the PTV data and are shown in Table 2, also. From this table, the measured values for the relative velocities in various concentration periods were in reasonable agreement with the calculated values using the R–Z correlations. One should not be surprised at this comparison. The R-Z empirical law is based on overall integral type measurements. The present effort indicates that it is indeed correct if you experimentally measure the solid and fluid average velocities and obtain the relative velocity from these.

The mean velocity of the two-phase flow can be calculated as

$$U_{ave} = U_f(1-\varepsilon_p) + U_p\varepsilon_p$$

and is compared with the velocity U_{LDA} measured using the LDA system with the presence of the beads. Fig. 8 shows the comparisons of U_r, U_{ave} and U_{LDA} from the LDA and PTV measurements. The velocities of fluid with beads measured by LDA are close to the values of U_{ave} at very dilute bead concentrations, whereas those corresponding to the higher bead concentration are closer to U_r, rather than U_{ave}. This may be explained by noting that the bead

Table 2
The relative velocities from the measurements and the Richardson and Zaki correlation

	Particle volume fraction (ε_p)	U_r, calculated from R–Z (cm/s)	U_r, calculated from $U_f - U_p$ (cm/s)	U_p (cm/s)
Period Ia	0.04	22.01	16.48	13.1
Period Ib	0.08	20.75	20.45	10.42
Period IIa	0.05	21.7	22.0	7.89
Period IIb	0.02	22.7	20.91	8.07
Period III	0.005	23.13	21.08	7.46

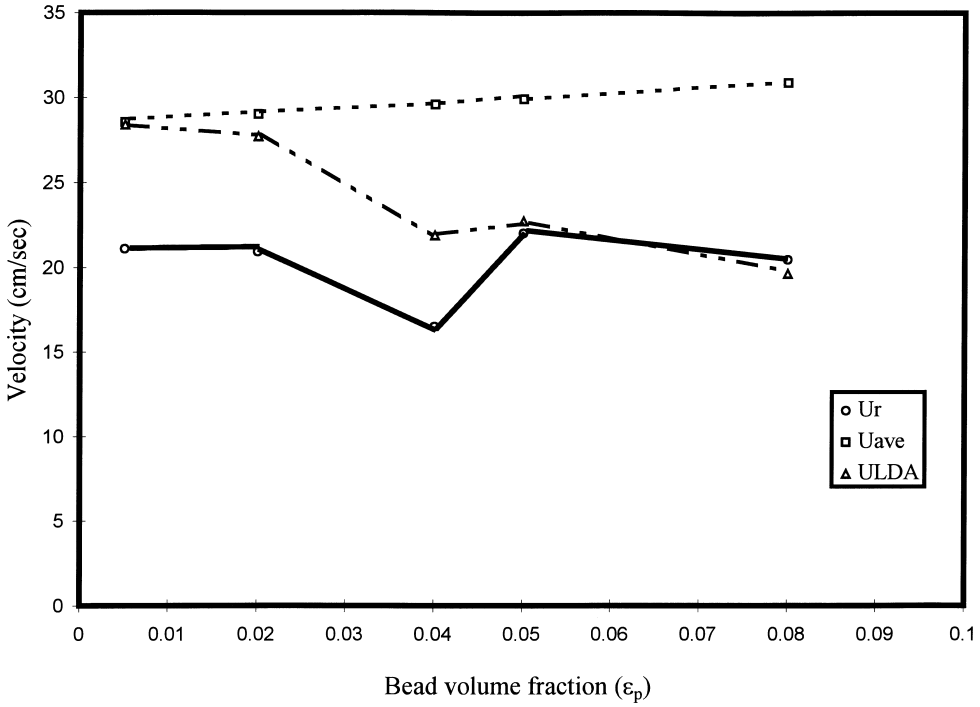

Fig. 8. Comparison of U_r, U_{ave} and U_{LDA} with bead volume fractions.

wake period (which corresponds to the U_r) dominates the flow system at higher concentration rather than the fluid period away from bead wake.

5.2. Comparison of the turbulent fluctuation in large particle two-phase flow with theories based on small particles

The theories for prediction of fluctuations in two-phase flow proposed by Hinze and Soo were based on the Stokes' law for small particles. Even though these theories are for the very small particles, it would be interesting to investigate how these apply to the data for the large particles. Hinze (1959) modified Tchen's theory (Tchen, 1961) with the assumptions of sinusoidally oscillating infinite element of the fluid and proposed the particle-to-fluid mean square velocity fluctuation terms as

$$\frac{u_p^2}{u_f^2} = \frac{\alpha T_L + \beta^2}{\alpha T_L + 1}$$

$$\alpha = \frac{36\mu_f}{(2\rho_p + \rho_f)d_p^2}$$

$$\beta = \frac{3\rho_f}{2\rho_p + \rho_f}$$

and T_L is the Lagrangian integral time scale (Brodkey, 1967).

Soo (1956) assumed that the very small particles follow the fluid. He further assumed that Stokes' law would be valid for the relative motion of particles and fluid so that the average fluid and particle velocities were the same. The relationship between the turbulent intensity for particles and fluid that he obtained was

$$\left(u_p^2/u_f^2\right)^{1/2} = \left(\pi^{1/4}/K^{1/2}\right)(\text{erf } K^{-1}) \exp\left(1/2K^2\right)$$

$$K = \left(Re_p/9\right)(d/\lambda)\left[1 + \left(\rho_f/2\rho_p\right)\right]\left(\rho_f/\rho_p\right)$$

λ is the microscale Lagrangian correlation and Re_p is the particle Reynolds number. The local fluctuations with the beads present as measured by LDA were used for the term, u_f', since a value of u_f' is not available that is not affected by bead wake. The Lagrangian integral scales and microscales were computed based on the k–ε model and Corrsin's relationship of microscale and integral scale for isotropic turbulence. These estimations are of course, rough. The fluctuations of the particles were calculated with the measured fluctuation of the fluid and are shown in Fig. 9. Hinze's predictions show that the dependence of the particle fluctuations on the concentration is steeper than the experimental and Soo's prediction. Hinze's prediction is closer to the experimental value than Soo's. Soo's equation predicts very low particle fluctuations. Even though Hinze's equation produced better results, the deviation from the experimental measurement is large. The inverse procedure was also tested, where the fluctuations of the fluid were calculated using the measured particle fluctuations. The results are not shown here (see Haam and Brodkey, 1998) and are similar to the particle fluctuation in Fig. 9. It is not surprising that Hinze's equation predicts closer fluctuation of the fluid to the experimental results rather than Soo's. These two theories predict the fluctuations in two-phase

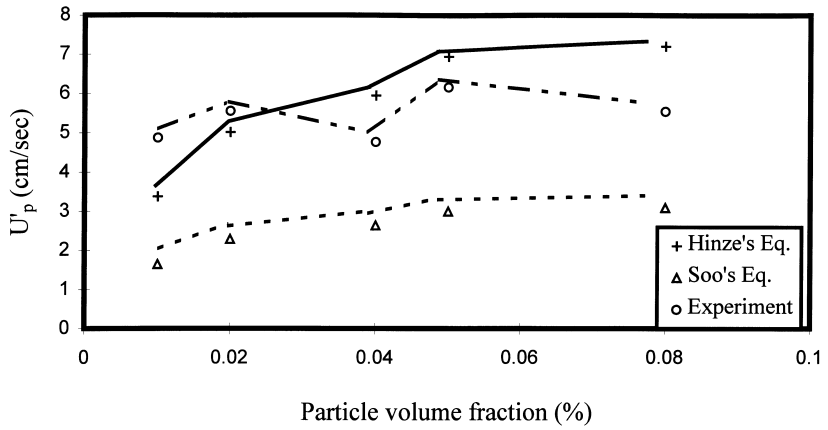

Fig. 9. Comparison of particle fluctuations on the particle concentration.

flow based on Stokes' law for very small particles are not the best for the large particle case, but could be used for rough estimates. Do not forget that these two theories were never meant to be used with data such as ours.

5.3. Large particle-turbulence interactions in dilute two-phase flow by Hestroni

Yarin and Hestroni's theory takes into account two source of turbulence in particle–fluid flow: (1) the carrier fluid velocity gradients and (2) the turbulent wakes behind the large particles. Their description of turbulence is based on a modified turbulent mixing length and the turbulent kinetic energy balance. The proposed theory is used to predict the turbulent fluctuation of the two phases according to the particle size and concentration. The final result for the effect of the wake of the particles is

$$\frac{(u')^{1/2}}{U_r} = (52.55\Omega)^{0.5}\left(\frac{\gamma}{\rho_{pf}} C_D^{3/2}\right)^{4/9}$$

where $C_D = (24/Re_p)(1 + 0.15Re_p^{0.687})$ as presented by Boothroyd (1971), $\gamma = m_p/m_f$, $\rho_{pf} = \rho_p/\rho_f$, and Ω is an empirical constant of the order of unity which accounts for the ratio of the maximum particle wake length to the spatial region of influence of the particle or bead.

The denominator, U_r, is the relative velocity, $u_f - u_p$, so that the data of relative velocities are required to compare the experimental data with the equation. However, the measurement of relative velocity is normally not available. It can be estimated when the experimental condition is that the fluid is at rest and the particles are falling. In our case, the relative velocity can be estimated with the data of the velocity measured by LDA and the velocity of the bead by PTV shown previously ($U_r = U_c - U_p$).

For the axial fluctuations, Fig. 10 shows that the 4/9 power law is fairly well matched with the experimental data. We include also the comparison for the radial fluctuations of the carrier

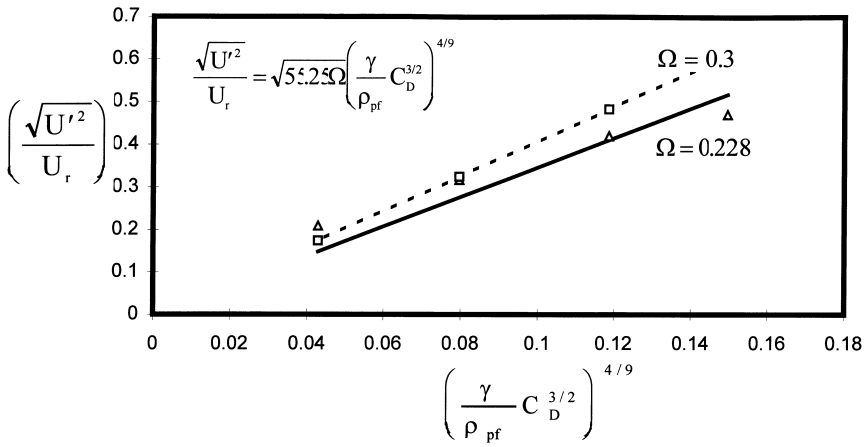

Fig. 10. Dependence of the carrier fluid fluctuation velocity (axial) on the complex $[(\gamma/\rho_{pf})C_D^{3/2}]^{4/9}$ using $U_r = U_c - U_p$ (from PTV).

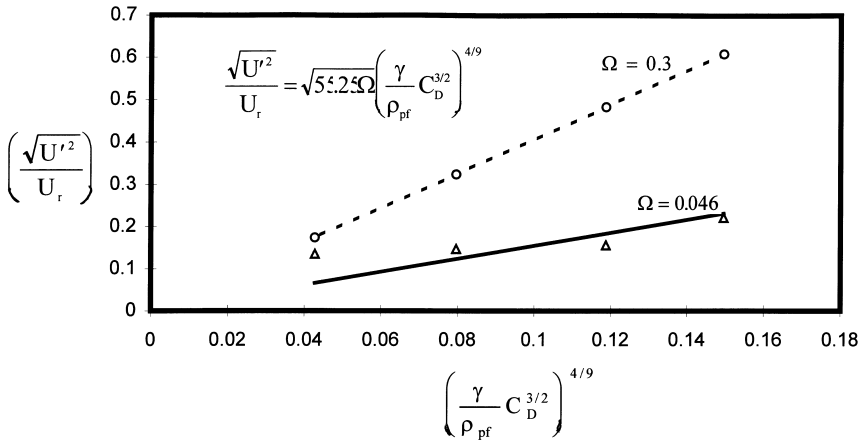

Fig. 11. Dependence of the carrier fluid fluctuation velocity (radial) on the complex $[(\gamma/\rho_{pf})C_D^{3/2}]^{4/9}$ using $U_r = U_c - U_p$ (from PTV).

fluid, Fig. 11, because this is the only theory that can be directly compared to our experimental results. The radial fluctuations show more scatter but the data are still in the 4/9 power range. Yarin and Hestroni computed the constant Ω for a homogeneous flow system as 0.36 with the data from Parthasarathy and Faeth (1990) and for pipe flow as 0.6 with the data from Tsuji et al. (1984). The corresponding constant Ω for our data was about 0.23 (see Fig. 10) for the axial fluctuations. For the radial fluctuations, the constant Ω was 0.05, which is very small when compared to Yarin and Hestroni's and that for the axial fluctuation. From Fig. 10, it is noted that the radial fluctuations of the carrier fluid do not strongly depend on the mass loading ratio which corresponds to the bead concentration.

6. Conclusions

The PTV system, accompanied by an image enhancement algorithm, proved to be the best choice for studying solid movement. Particle overlapping was a major limitation especially for the high concentration period; however, with the added algorithm, up to 95% of the total overlapped particles in a single image could be decompose. The use of the PTV system also provided the concentration measurement. The PTV algorithm produced very accurate particle counts (concentration) in the concentration level from low to moderate periods. Even for high concentration period, the PTV algorithm were able to measure the concentration with an accuracy of 95%.

The data at high concentrations showed high axial and radial rms velocity values of the beads; however, these increases were relatively less than that for the fluid phase. The axial turbulent intensity values at the lowest concentration periods (III) was about 65 and 78% in region II, the highest concentration period after the beads were fully dispersed. The higher intensity for the solid phase relative to the fluid phase is a result of the intensity being calculated as a percentage of the mean of the respective phase. Thus, since the mean solids

velocity is much less than for the fluid, the intensity is higher even though the rms values were lower. The concentration effect on the beads fluctuation is less for the radial component than for the axial component, which is similar to that for the fluid phase. From the results of the histogram analysis, the higher bead concentration period provided broader and more scattered distributions except for the initial transport period. The dependency of the level of turbulent intensity on the concentration reflects the broader distributions even though the differences are less for the fluid phase.

From the integral analysis based on the Richardson and Zaki correlation, the velocities measured by the LDA technique, U_{LDA}, were close to the values of U_{ave}, which was calculated for the diluted bead concentration periods. In contrast, those that correspond to the higher bead concentration were close to U_r rather than U_{ave}. This may be explained by noting that the bead wake region (which corresponds to the U_r) dominates the low system at higher concentrations rather than the fluid region away from bead wake.

An attempt to use the experimental data for large particles to compare with the classical two-phase models for small particles proposed by Soo and Hinze showed significant deviations as expected. However, the Hinze approach can be recommended as a useful estimate. The 4/9 power law model for large particle proposed by Yarin and Hestroni, which is believed to be the only reliable theory for the large particle system, was well matched with the experimental data for the axial fluctuations. The radial fluctuations of the carrier fluid showed more scatter, but the data were still in the 4/9 power law range.

Acknowledgements

The authors wish to thank the National Science Foundation for an International Cooperative Grant with the Czech Republic for the support of this work. The support of the Department of Chemical Engineering for S.J. Haam throughout the two periods that he studied in Columbus is also greatly appreciated.

References

Boothroyd, R.G., 1971. Flowing Gas-Solids Suspensions. Chapman & Hall, London.

Brodkey, R.S., 1967. The Phenomena of Fluid Motions. Addison-Wesley, MA.

Choi, W.C., Guezennec, Y.G., Brodkey, R.S., 1992. In-situ calibration on stereo matching for 3D particle image velocimetry. Bulletin of American Physical Society 36, abstract only.

Govan, A.H., Hewitt, G.F., Ngan, C.F., 1989. Particle motion in a turbulent pipe flow. Int. J. Multiphase Flow 15 (3), 471–481.

Guezennec, Y.G., Brodkey, R.S., Trigui, N., Kent, J.C., 1994. Algorithm for fully automated three-dimensional particle tracking velocimetry. Exp. in Fluids 17, 209–219.

Haam, S., 1996. Multiphase research on solid–liquid dispersion. Ph.D. Dissertation, Department of Chemical Engineering, The Ohio State University.

Haam, S.J., Brodkey, R.S., 1998. Motions of dispersed beads obtained by particle tracking velocimetry measurements. (http://www.er6.eng.ohio-state.edu/~brodkey/curnot.htmlx).

Hinze, J.O., 1959. Turbulence. McGraw-Hill, New York.

Koh, C.J., Hookham, P., Leal, L.G., 1994. An experimental investigation of concentrated suspension flows in a rectangular channel. J. Fluid Mech 266, 1–32.

Mondy, L.A., Giraham, A.L., Majumdar, A., Bryant Jr., L.E., 1986. Technique for measuring particle motions in concentrated suspensions. Int. J. Multiphase Flow 12, 497–502.

Nouri, J.M., Whitelaw, J.H., 1992. Particle velocity characteristics of dilute to moderate dense suspension flows in stirred reactors. Int. J. Multiphase Flow 18, 21–33.

Parthasarathy, R.N., Faeth, G.M., 1990. Turbulence modulation in homogeneous dilute particle-laden flow. J. Fluid Mech 220, 485–537.

Shriber, A.A., Gavin, L.B., Naumov, V.A, Yatsenko, V.P., 1990. Turbulent Flow in Gas Suspension. Hemisphere, New York.

Shuen, J.S., Solomon, A.S., Zhang, Q.F., Faeth, G.M., 1985. Structure of particle-laden jet: measurements and predictions. AIAA Jour 23, 396–404.

Soo, S.L., 1956. Statistical properties of momentum transfer in two-phase flow. Chem. Eng. Sci 5, 57–67.

Tchen, C.M., 1961. Mean value and correlation problems connected with the motion of small particles suspended in a turbulent fluid. Ph.D. Thesis, Martinus Nijhoff, Delft, The Hague.

Tsuji, Y., Morikawa, Y., Shiomi, H., 1984. LDV-measurements of air–solid two-phase flow in a vertical pipe. J. Fluid Mech 120, 358–409.

Yarin, L.P., Hestroni, G., 1994. Turbulence intensity in dilute two-phase flow-3. Int. J. Multiphase Flow 20, 27–44.

Yuan, Z., Michaelides, E.E., 1992. Turbulence modulation in particulate flows — a theoretical approach. Int. J. Multiphase Flow 18, 779–785.